

Cyclic Energy Dissipation of Thin-Walled Cold-Formed Steel Structural Elements



D. Padilla-Llano, M. R. Eatherton & C. D. Moen

Civil & Environmental Engineering, Virginia Tech

SUMMARY:

Design of cold-formed steel (CFS) structures subjected to lateral seismic force has traditionally focused on the behavior of lateral resisting subassemblages such as strapped/sheathed shear walls or tubular diagonal braced frames (e.g. HSS). However, tests on these subassemblages give limited information about the seismic performance of actual cold-formed steel structures. To model and thus predict the seismic performance of CFS buildings, it is necessary to develop accurate and computationally efficient hysteretic models of individual components and connections in CFS buildings. This paper presents experimental results from monotonic and cyclic axial tests on cold-formed steel members. Column length and cross-section dimensions are varied to investigate the influence of local, distortional and global buckling strength limit states on cyclic load-deformation response. A pinching hysteretic model is then developed to capture key aspects of the experimental cyclic behavior including strength degradation, stiffness degradation, and energy dissipation of common cold-formed steel structural studs.

Keywords: Cold-formed steel, hysteretic behavior, energy dissipation, buckling, seismic behavior

1. INTRODUCTION AND MOTIVATION

In the past twenty years, performance based earthquake engineering has caused a dramatic shift in the way engineers and researchers approach seismic design. Whereas the focus of earthquake engineering used to be providing a minimum level of protection against collapse using a set of prescriptive requirements, the focus has shifted toward a more detailed understanding and control over the seismic performance of a structure. Because there is a wide range of possible building geometries and structural layout, it is necessary to have a set of computational tools that can be used to model many different structural configurations. Furthermore, because of the variability in ground motions, it is often necessary to consider a suite of ground motions to adequately characterize the behavior of a structure subjected to a given hazard level. To develop seismic performance factors to use in design, it can be necessary to vary both structural configuration, ground motions, and ground motion intensity resulting in thousands of computational analyses (FEMA 2009). Computationally efficient tools are therefore crucial.

Seismic analysis and design of cold formed steel (CFS) structures is based on the cyclic testing of subassemblages such as sheathed shear walls or strapped frames. The design of CFS lateral load resisting systems for buildings is conducted using prescriptive design tables based on the subassemblage tests. Although this design method is expected to provide adequate protection against collapse during earthquakes, it provides little information about the seismic behavior of the actual CFS structures. Actual CFS buildings include odd geometry (e.g. intersecting walls), load transfer mechanisms not included in tests, and many gravity resisting elements and connections.

To facilitate performance based earthquake engineering of CFS structures, and to better understand their expected seismic behavior, it is necessary to develop accurate and computationally efficient

models of CFS elements and their connections. This paper describes one phase of a larger effort to experimentally characterize the cyclic behavior of CFS elements and connections. CFS studs were subjected to cyclic axial displacement histories. A pinching hysteretic model was then developed to capture salient features of the experimental cyclic behavior including unique tension and compression backbone, strength degradation, stiffness degradation, and energy dissipation of common CFS structural studs.

Figure 1a shows typical CFS framing including studs, bottom tracks, top tracks, and diagonal strapping. Figure 1b demonstrates the concept for simulating the CFS framing using a toolbox of hysteretic springs to represent each of the elements and connections. This paper presents the experimental calibration of the pinching model selected to simulate the axial behavior of the studs.

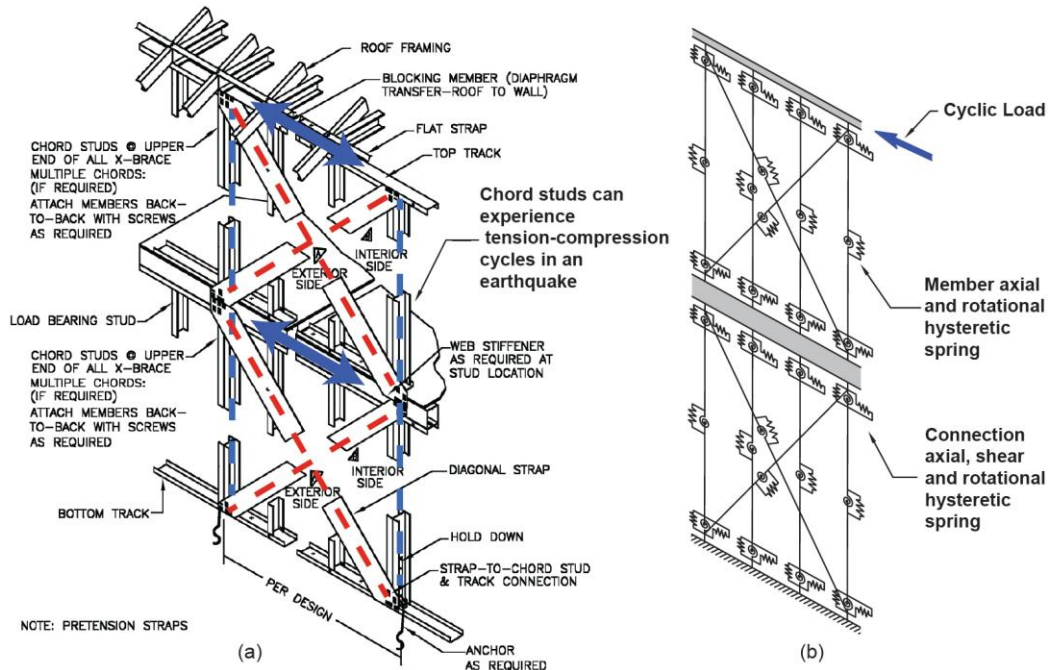


Figure 1. (a) Typical Cold-Formed Steel Framing (from SFA 2000) and (b) Simplified Phenomenological Model of the Same Structure

3. EXPERIMENTAL PROGRAM

An experimental program was conducted at the Thomas M. Murray Structural Engineering Laboratory at Virginia Tech, aimed at studying the response of cold-formed steel C-shaped studs subjected to cyclic axial load.

3.1. Testing program and Experimental Setup

Cold-formed steel members under compression can experience local, distortional or global (euler) buckling depending on their elastic buckling properties. Their cyclic behavior will also be different depending on the buckling mode. A set of 24 tests were performed to examine the behavior of C-shaped studs that are expected to be governed either by local, distortional or global buckling as predicted by the AISI Direct Strength Method (AISII 2007). The test specimens were varied in cross-section dimensions and length in order to isolate each limit state. Studs with two different web depths (92mm and 152 mm) were selected.

Cross section dimensions were measured at the mid-height using methods described in Moen (2008). These values were used to calculate the elastic buckling loads (P_{crb} , P_{crd} , P_{cre}), and their corresponding half-wave lengths (L_{crb} , L_{crd}) using the finite strip eigen-buckling analysis in CUFSM (Ádány and

Schafer 2004). The yield load P_y was determined using measured section area and the average yield stress obtained from three coupon tests per specimen conducted in accordance with ASTM E8M-04 (ASTM 2004). Finally the compression capacity, P_n , was predicted for each specimen using the AISI Direct Strength Method (DSM). These values will be used later in this paper.

The test matrix includes two quasi-static cyclic tests and two monotonic tests per specimen type. The monotonic tests were performed to establish a backbone for comparison to the cyclic response to determine strength degradation parameters. The test matrix is summarized in Table 1.

Table 1. Test Matrix

Specimen	Limite State	L (mm)	Web width (mm)	Flange width (mm)	Thickness (mm)	# Cyclic Test	# Monotonic Test
362S162-54-LA#	Local	305	92	41	1.44	2	2
600S162-33-LA#	$(\lambda_f \gg \lambda_d, \lambda_c)$	305	152	41	0.88	2	2
362S137-68-DA#	Distortional	610	92	35	1.81	2	2
600S137-68-DA#	$(\lambda_d \gg \lambda_f, \lambda_c)$	610	152	35	1.81	2	2
362S137-68-GA#	Global	2286	92	35	1.81	2	2
600S137-97-GA#	$(\lambda_c \gg \lambda_f, \lambda_d)$	2286	152	35	2.58	2	2

A= Axial, G= Global, D= Distortional, L= Local, # indicates Cyclic or Monotonic

The unidirectional loading rig is shown in Figure 2. The reaction frame includes two braces to prevent the lateral sway and twist of the actuator and top attachment plate respectively. A prescribed cyclic displacement history was applied using a servovalve controlled hydraulic actuator. End plates were welded to both ends of the specimen to transfer axial forces while providing a fixed end boundary condition with fixed warping restraint. The average of two LVDT transducers was used to control the test displacement. These transducers were connected between the top and bottom end plates to accommodate an accurate measurement of the axial displacement without the influence of the end plate deformation. This is shown on the right of Figure 2. A constant loading rate of $800 \mu\epsilon/\text{min}$ was used for the cyclic tests and the loading rate for the monotonic test was set to 21MPa per minute.

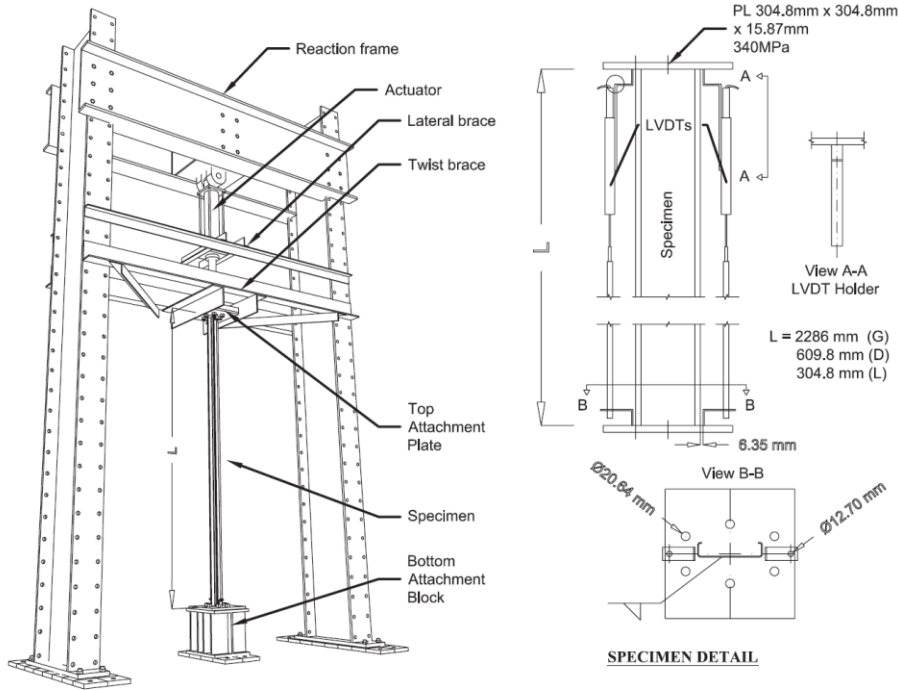


Figure 2. Test setup and specimen detail.

Additional instrumentation was provided to capture the specimen behavior including a set of 8 or 16

string potentiometers and between 750 and 1800 photogrammetry targets. This instrumentation will be used to analyse the buckling deformations including measuring the buckling half-wave lengths and decomposing the contribution of each buckling mode to the deformed shape. However, the data related to this instrumentation is not necessary for the purposes of this paper and thus is not presented.

3.2. Cyclic Loading Protocol and Instrumentation

The objective of a cyclic seismic loading protocol is to simulate the number of inelastic cycles, cumulative inelastic demand, and peak displacement demand associated with a design seismic event (Krawinkler 2009). However, the axial demand in a cold-formed steel member depends on many factors such as the location of the member in the building, end connections, ground motion properties, dynamic properties of the building, and others. The objective of the loading protocol presented herein was therefore focused on characterizing hysteretic behavior and associated progression of damage states rather than reproducing seismic demands for a specific configuration.

The loading protocol was adapted from the FEMA 461 quasi-static cyclic deformation-controlled testing protocol (FEMA 2007). The FEMA 461 loading protocol was developed by statistical analysis of story drift demands from nonlinear response history analyses on SDOF and MDOF frame structures subjected to 20 non-near fault ground motions. This protocol is intended to simulate the cycles leading up to a peak deformation, rearranged in order of increasing amplitude. There are two cycles per deformation step and the FEMA document suggests three deformation steps before reaching the lowest damage state. The displacement protocol therefore includes three displacement steps prior to the predicted initiation of buckling deformations. The fourth displacement step is set to be the displacement δ_e corresponding to the load P_e that will initiate buckling in the member. The buckling displacement, δ_e is calculated using Eqn. 3.1 as a function of the member slenderness, $\lambda=(P_e/P_{cr})^{0.5}$ for an applied load P_e , and critical elastic buckling load, P_{cr} .

$$\delta_e = \lambda^2 P_{cr} \frac{L}{AE} \quad (3.1)$$

The load, P_e , that initiates buckling for local and distortional buckling is taken as is $0.60P_{cr\ell}$ and $0.31P_{crd}$ respectively, which corresponds to the AISI (2007) limit values of λ_ℓ and λ_d . For global buckling, the load that initiates global buckling deformation is assumed to be $P_e = 0.5P_{cre}$ which corresponds to a slenderness value of 0.71. Figure 3 shows the proposed loading protocol. The use of a symmetric protocol with equal deformation demands in compression and tension was selected in order to capture the damage and energy dissipation due to cross-sectional deformations of thin-walled channel section under compression and the damage and cracking that can occur by the reversal of these deformations under tension loading.

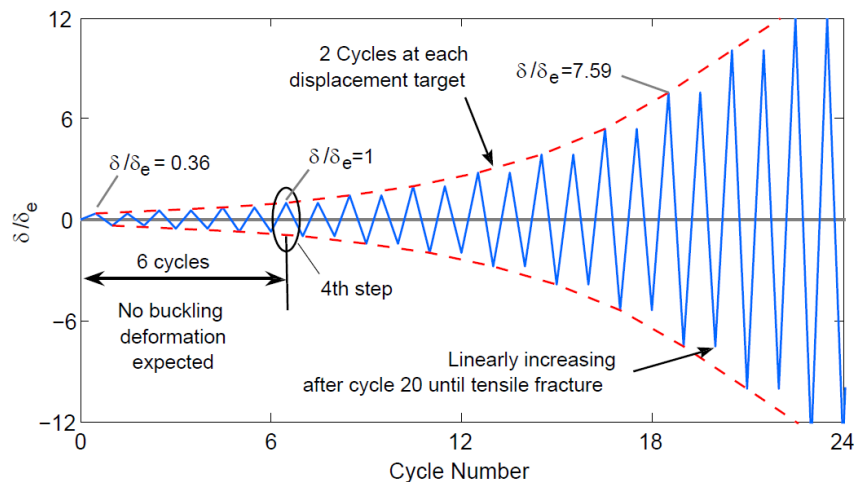


Figure 3. Cyclic compression-tension cold-formed steel loading protocol

4. EXPERIMENTAL RESULTS

4.1. Global Buckling Results

The global buckling specimens exhibited weak axis flexural buckling which led to folding of the stiffening lips near the mid-height as shown in Figure 4b and local web buckling near the supports at the points of reversed curvature. Damage due to reversal of the strains accumulated at the folded lips as subsequent excursions in tension and compression took place. As shown in Figure 4, the compression strength degrades rapidly after the peak load P_{min} is reached, yet post-buckling energy dissipation is still observed after this point. The tension excursions are characterized by low stiffness until the member straightens out, then ductile yielding at a fairly consistent tension yield capacity. The final failure mode was gradual tearing of the section starting at the folded lips and propagating through the cross section, or in some cases fracture near the welded connection.

The monotonic tests were also characterized by weak axis flexural buckling, with folding of the stiffening lips at the mid-height. One specimen, 362S137-68-GAM-2, exhibited a flexural torsional buckling mode failure due to torsional initial imperfections in the member. The difference between the monotonic behavior (600GAC-1) and envelope of the cyclic behavior (600GAC-1) shown in Figure 4a is strength degradation due to damage accumulation. The strength degradation will be characterized as part of this study.

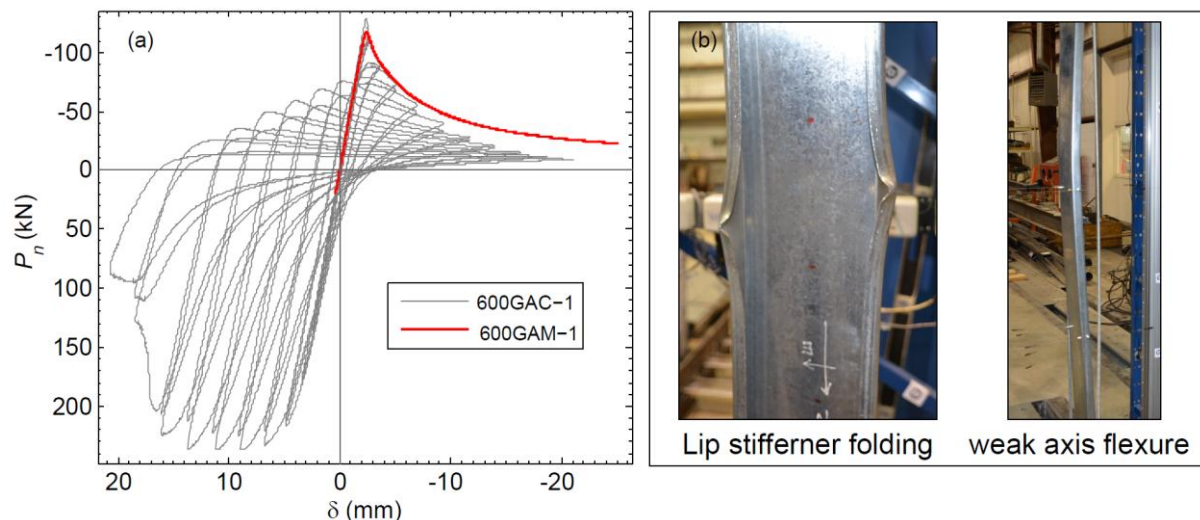


Figure 4. Specimen 600S137-97-GAC-1 and 600S137-97-GAM-1 Demonstrating Global Buckling:
(a) Hysteretic and Monotonic Behavior and (b) Picture of Buckling Mode

4.2. Distortional Buckling Results

The cyclic response of the 600S137-68-DAC-# distortional buckling specimens was characterized by the formation of at least one distortional buckling half-wave length centred at mid-height as shown in Figure 5b. The compressive strength degradation occurred more gradually for distortional buckling than for global buckling. Damage was observed to accumulate at the round corners where inelastic strain concentrated as the member stretched and compressed. The strength in tension remained relatively constant until tears started forming at the round corner which finally propagated through the cross section. The cyclic response of 362 distortional buckling specimens was characterized by fewer cycles before fracture (approximately half in some cases). The buckling deformations were a combination of distortional and local buckling of the web near one of the end plates. The hysteric behavior was found to be more similar to the local buckling specimens and is therefore not shown here.

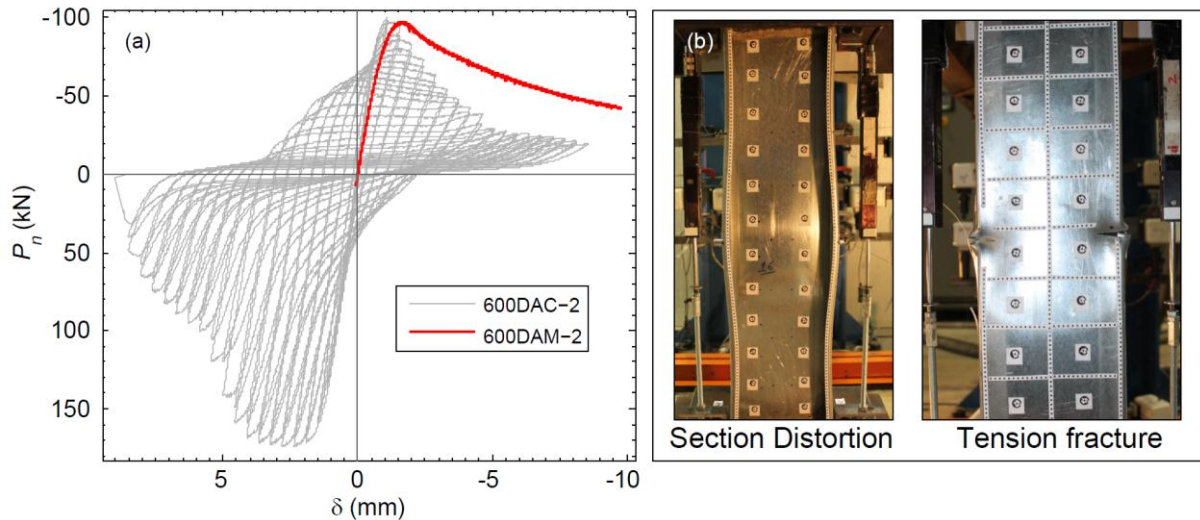


Figure 5. Specimen 600S137-68-DAC-2 and 600S137-68-DAM-2 Demonstrating Distortional Buckling: (a) Picture of Buckling Mode and (b) Hysteretic and Monotonic Behavior

4.3. Local Buckling Results

The cyclic response of the 362 local buckling specimens was characterized by web buckling in compression with at least two half-waves occurring before reaching the peak load P_{min} . After the peak compression load the buckled shape became constant with one half-wave buckle around mid-height. Damage then accumulated at the mid-height local buckle. The compressive strength degraded quickly after peak load as well as the unloading stiffness on the compression side. The tensile strength degraded more than the distortional and global buckling specimens. The members finally fractured by tearing that initiated at the web and propagated around the cross section. The monotonic response of the specimens demonstrated similar deformations as their cyclic counterpart; however the deformations were localized closer to the top end plate. Both cyclic and monotonic exceeded the predicted compressive capacity P_n but reached maximum values in tension below to the yield load P_y .

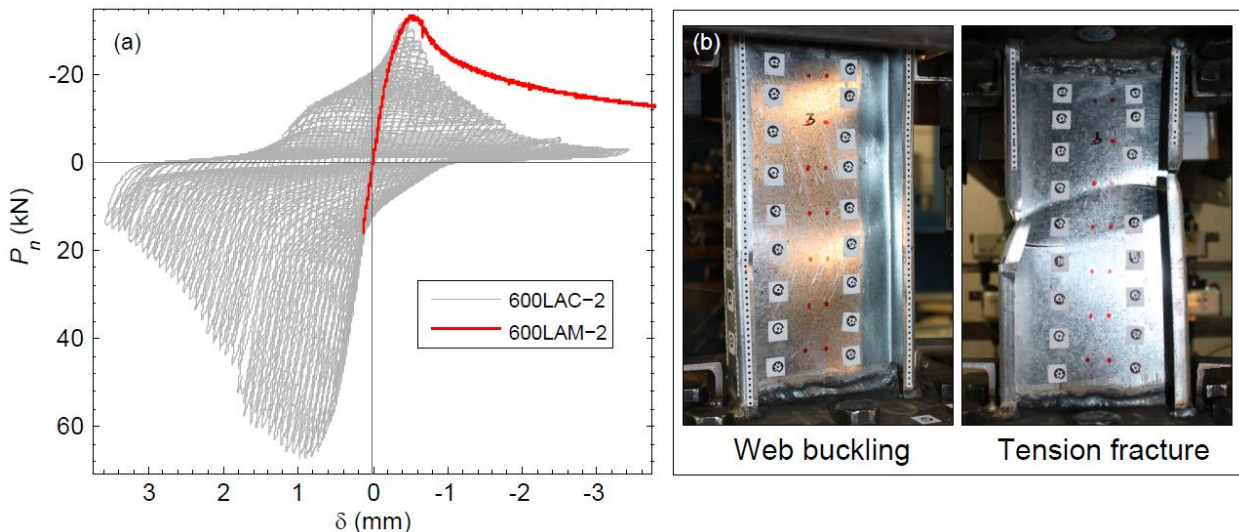


Figure 6. Specimen 600S162-33-LAC-2 and 600S162-33-LAM-2 Demonstrating Global Buckling: (a) Picture of Buckling Mode and (b) Hysteretic and Monotonic Behavior

The response of the 600 local buckling specimens was characterized by web buckling in compression with two half-wave lengths occurring before peak load P_{min} . After peak load two yield lines formed around mid-height as shown in Figure 6b and damage accumulated there. Strength and stiffness degraded in a similar fashion as described above, however the specimen underwent several cycles

before exhibiting any tearing of the section. The tensile fracture started occurring at the web close to the rounded corners where the two yield lines met and propagated to the flanges.

4.4. Comparison of the Energy Dissipation of the three limit states

The amount of hysteretic energy dissipated per cycle and the cumulative total is shown in Figure 7. The cumulative hysteretic energy, HE_c , was normalized to the reference energy, E_{TR} , which is approximately the energy dissipated by an equivalent perfectly elastic element with compression capacity P_n and tensile capacity P_y . The reference energy, E_{TR} , is calculated using equation (4.1). The normalized hysteretic energy per cycle, NHE_{pc} , was normalized to the reference energy, E_{CR} , given by equation (4.2) and depicted in the inset of Figure 7b.

$$E_{TR} = (P_n^2 + P_y^2)(L/2AE) \quad (4.1)$$

$$E_{CR} = (P_n + P_y)(\delta_{min}^i + \delta_{max}^i) \quad (4.2)$$

It can be seen that the energy dissipation characteristics per cycle for global buckling (GAC specimens) are similar for both cross sections; however, the bigger cross sections (i.e. 600GAC specimens) start dissipating energy earlier in the displacement protocol. For distortional buckling, the difference is more evident. The 362DAC specimens exhibited coupled buckling distortional and local deformations and thus their behavior is more similar to the 362 local buckling specimens. The level of dissipated energy per cycle for the local buckling specimens shows a noticeable difference between the two cross section sizes. The 600LAC specimen dissipated more energy through elastic buckling of the web in contrast to the 362LAC specimens in which most of the dissipation was due to inelastic deformations caused by folding of the section.

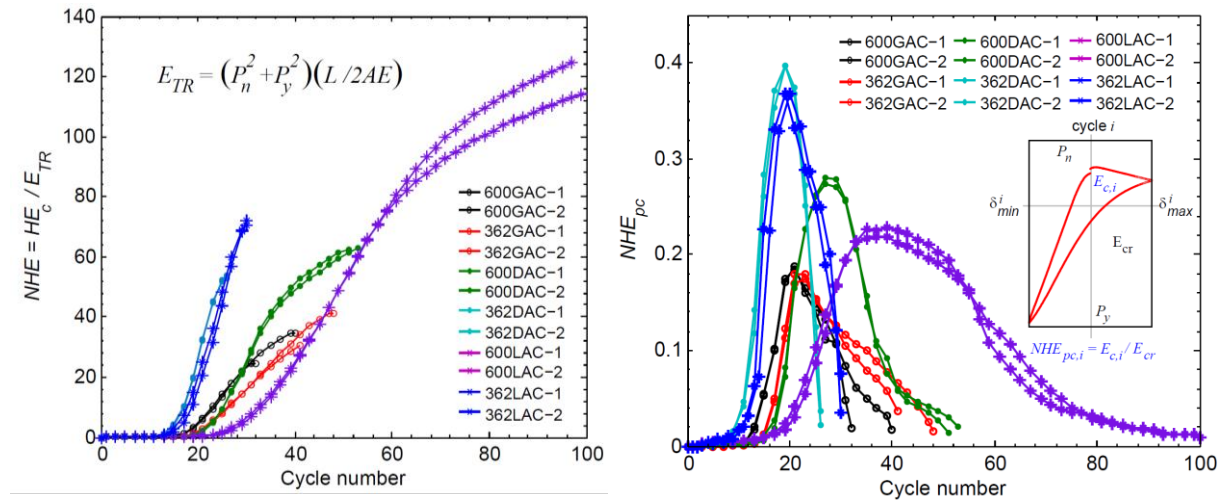


Figure 7. Normalized Hysteretic Energy Dissipated.
(a) Cumulative and (b) Per Cycle

5. HYSTERETIC MODELING

The need for accurate and computationally efficient hysteretic models for CFS members and connections was described at the beginning of this paper. Hysteretic models that are capable of accurately simulating the behavior will need to capture the unique nature of the tension and compression backbones, strength degradation, stiffness degradation, and pinching hysteretic shape.

Backbone curves were defined for the monotonic test results using a modified version of the method used by Ayhan and Schafer (2012). Ayhan and Schafer (2012) characterized the moment-rotation response of monotonically loaded cold-formed joists and provided some expressions for the backbone.

Their expressions consider a multi-linear model that includes a vertical drop of the strength after the post-peak value. However, this formulation may lead to convergence problems when implementing in software for nonlinear response analyses and it does not reflect the actual post-peak behavior shown above. Therefore, the backbone curve used in this work includes a softening branch to simulate the obtained monotonic response. The more accurate post-peak behavior also allows the use of deterioration models such as the one proposed by Ibarra et al. (2005).

The procedure for fitting a backbone curve utilizes a least squares method for minimizing the error between the energy dissipated in the monotonic tests and the equivalent energy dissipated using the multi-linear model. Herein a quad-linear model as depicted in Figure 8a is fit to the normalized monotonic response. As suggested by Ayhan and Schafer, the fit is performed for pre and post peak energy separately to prevent over or under compensation of the dissipated energy. Additional constraints were provided such that the fitted model preserved the shape of the experimental results. The point (δ_2, P_2) was fixed to the maximum load P_{min} (and corresponding displacement) and point (δ_4, P_4) was set to the last data point recorded. The fitted points are summarized in Table 2. An example of the fitted backbone model is shown in Figure 8b.

Table 2. Normalized Definitions for Compression side of Backbone

Specimens	δ_e ($\times 10^{-3}$ mm)	P_y (kN)	Compression Side												Area Error $\times 10^{-7}$
			δ_1/δ_e	δ_2/δ_e	δ_3/δ_e	δ_4/δ_e	P_1/P_y	P_2/P_y	P_3/P_y	P_4/P_y	k_1	k_2	k_3	k_4	
600S137-97-GAM-1	-	-	3.1	3.7	9.1	38.6	0.433	0.482	0.210	0.094	140.4	73.6	-51.0	-3.9	0.307
600S137-97-GAM-2	-	-	3.1	4.5	11.8	38.8	0.373	0.414	0.209	0.105	121.9	28.8	-28.2	-3.8	0.044
362S137-68-GAM-1	-	-	3.0	4.3	10.8	39.8	0.414	0.460	0.237	0.122	136.1	37.2	-34.1	-4.0	1.756
362S137-68-GAM-2	-	-	2.9	3.7	10.6	39.4	0.391	0.435	0.182	0.083	133.6	53.6	-37.1	-3.4	0.942
Average			3.0	4.1	10.6	39.2	0.403	0.448	0.209	0.101	133.0	48.3	-37.6	-3.8	0.762
COV			0.02	0.09	0.11	0.01	0.07	0.07	0.11	0.16	0.06	0.41	0.26	0.07	-
600S137-68-DAM-1	173	91	6.2	10.6	27.5	45.0	0.493	0.548	0.381	0.283	79.6	12.6	-9.9	-5.6	0.078
600S137-68-DAM-2	173	90	5.7	9.5	28.7	57.0	0.495	0.549	0.353	0.237	87.4	14.2	-10.3	-4.1	0.287
362S137-68-DAM-1	-	-	2.5	3.3	6.8	16.8	0.735	0.816	0.540	0.362	293.2	98.3	-79.4	-17.9	0.218
362S137-68-DAM-2	-	-	2.0	2.8	6.7	17.5	0.724	0.804	0.538	0.341	356.4	103.5	-68.7	-18.3	0.214
Average			4.1	6.6	17.4	34.1	0.612	0.679	0.453	0.306	204.2	57.1	-42.1	-11.5	0.199
COV			0.52	0.62	0.71	0.59	0.22	0.22	0.22	0.18	0.69	0.89	0.88	0.67	-
600S162-33-LAM-1	33	27	8.1	12.6	48.0	159.0	0.385	0.427	0.235	0.136	47.3	9.5	-5.4	-0.9	1.353
600S162-33-LAM-2	48	32	6.3	11.5	28.0	109.2	0.416	0.462	0.255	0.148	66.0	8.9	-12.5	-1.3	1.599
362S162-54-LAM-1	231	81	2.7	3.5	8.5	23.5	0.699	0.777	0.430	0.267	256.2	99.1	-69.5	-10.9	0.233
362S162-54-LAM-2	234	81	3.0	3.8	8.4	25.1	0.681	0.756	0.427	0.252	230.4	86.9	-72.2	-10.5	0.399
Average			5.0	7.9	23.2	79.2	0.545	0.606	0.337	0.201	150.0	51.1	-39.9	-5.9	0.896
COV			0.52	0.62	0.81	0.84	0.31	0.31	0.32	0.34	0.72	0.95	0.90	0.94	-

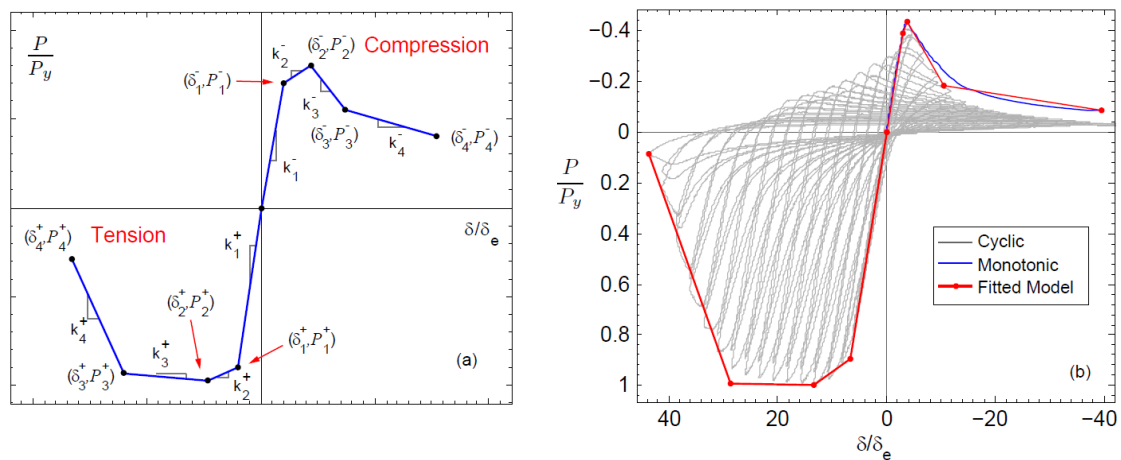


Figure 8. Backbone curve for hysteretic model used for CFS Member Axial Behavior
(a) Idealized model and (b) Backbone Model applied to specimen 362S137-68-GAC-2

The pinching model shown in Figure 9a based on Ibarra et al. (2005) was used found to simulate the

hysteretic behavior of the CFS members and was therefore selected. The strength and stiffness deterioration rules for this model are based on the dissipated hysteretic energy through a parameter β_i calculated for each excursion using Eqn. 5.1. For strength degradation, the backbone forces (given by F_i and F_{i-1} which are the degraded backbone force before and after excursion i respectively) are then modified after each excursion using Eqn. 5.2. Stiffness degradation takes a similar form as Eqn. 5.2.

$$\beta_i = \left(\frac{E_i}{E_t - \sum E_j} \right)^c \quad (5.1)$$

$$F_i^\pm = (1 - \beta_i) F_{i-1}^\pm \quad (5.2)$$

The energy dissipation parameter, β_i , is a function of the energy dissipated in excursion i , E_i , the cumulative energy dissipated in the previous excursions, $\sum E_j$, and the total available energy, E_t . The parameter c defines the rate of deterioration. These values are determined through calibration from the experimental results. A more in depth discussion of the model can be found in Ibarra et al. (2005). An example of a simulated hysteretic response is provided in Figure 9b. The simulation was performed in OpenSees (Mazzoni et al. 2009) using the *pinching4* uniaxial material model. This model, developed by Lowes et al. (2004), is essentially equivalent to the Ibarra et al. (2005) hysteretic model. The backbone curve was defined for specimen 362S162-54-LAC-2. The tension backbone points and parameters controlling pinching shape and strength degradation are listed in Table 3. The definition of the parameters related to the Pinching4 material model are given in Mazzoni et al. (2009). It is shown in Figure 9b that the calibrated pinching model can capture the cyclic hysteretic behavior of the tested specimen including strength degradation.

Table 3. Parameters for the *Pinching4* Model Example

uForceN	0.10	uForceP	-0.30	δ_1/δ_e	2.40	δ_3/δ_e	1.00
rForceN	0.90	rForceP	0.15	P_1/P_y	0.90	P_3/P_y	1.50
rDispN	0.98	rDispP	-0.10	δ_2/δ_e	7.70	δ_4/δ_e	16.30
gF2	5.60	gE(E_t)	143.13	P_2/P_y	1.15	P_4/P_y	1.20
gF4(c)	0.75	gFlim	10^5				

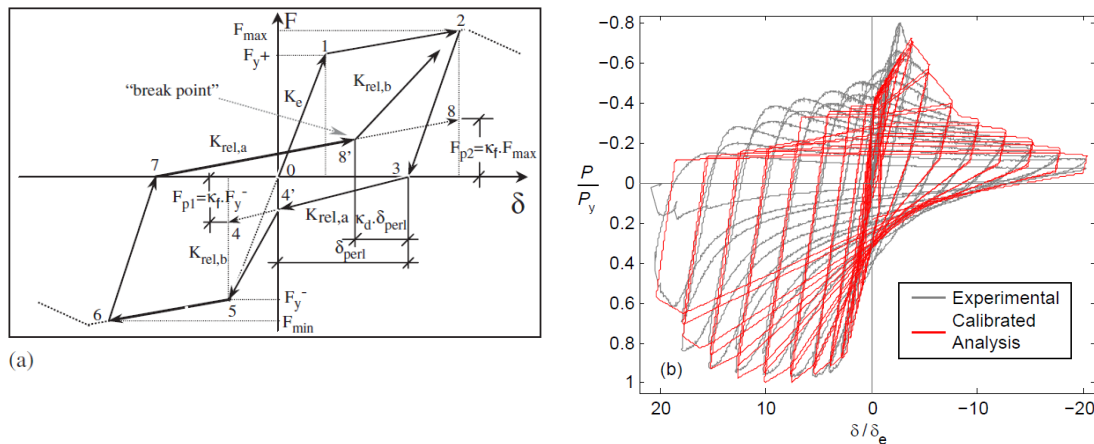


Figure 9. Simulated Hysteretic Response of Axial Behavior for CFS member

(a) Model Definition (Ibarra et al. 2005) and (b) Example of OpenSees pinching Model applied to specimen 362S162-54-LAC-2

6. CONCLUSIONS

To understand the seismic performance of cold-formed steel structures, it is critical to have modelling tools capable of simulating CFS members and connections as applied in many different configurations.

Furthermore, it is critical that these modelling tools be computationally efficient to allow the numerous analyses required to statistically assess the seismic performance of CFS structures. A research program is underway to build these computational tools. Toward that objective, this paper describes the testing and characterization of the cyclic axial behavior of CFS members. An experimental program was conducted including twelve monotonic and twelve cyclic tests. It was found that the different buckling modes have different energy dissipation and post-peak response. A pinching hysteretic model was then developed to capture the unique tension and compression backbone curves, pinching hysteretic shape, strength degradation, and stiffness degradation. An example of the calibrated hysteretic model demonstrated that this model can reasonably capture the salient features of CFS member cyclic response.

ACKNOWLEDGEMENT

The authors are grateful to the American Iron and Steel Institute for supporting this project, and to Clark Dietrich Building Systems for the specimen donations.

REFERENCES

- Ádány, S., Schafer, B.W. (2004). Buckling analysis of cold-formed steel members using CUFSM: conventional and constrained finite strip methods. *18th International Specialty Conference on Cold-Formed Steel Structures*, October 26-27, 2006, Orlando, Florida.
- American Iron and Steel Institute (AISI). (2007). North American Specification for the Design of Cold-Formed Steel Structural Members, Washington D.C.
- ASTM. (2004). E 8M-04, Standard Test Methods for Tension Testing of Metallic Materials (Metric). ASTM International, West Conshohocken, PA.
- Ayhan and Schafer (2012) Characterization of moment-rotation response of cold-formed steel beams. *Proceedings of the Annual Stability conference*, April 18-21, 2012, Grapevine, Texas.
- Calderoni, B., De Martino, A., Formisano, A., and Fiorino, L. (2009). Cold formed steel beams under monotonic and cyclic loading: Experimental investigation. *Journal of Constructional Steel Research*, 65(1), 219–227.
- FEMA (2007) Interim protocols for determining seismic performance characteristics of structural and nonstructural components through laboratory testing, Published by the Federal Emergency Management Agency, Document No. FEMA 461.
- FEMA (2009) *FEMA P695 - Quantification of Building Seismic Performance Factors*, Federal Emergency Management Agency (FEMA), Washington, D.C.
- Goggins, J., Broderick, B., Elghazouli, A., and Lucas, A. (2005). Experimental cyclic response of cold-formed hollow steel bracing members. *Engineering Structures*, 27(7), 977–989.
- Ibarra L., Medina, R., and Krawinkler, H. (2005). Hysteretic models that incorporate strength and stiffness deterioration. *Earthquake Engineering and Structural Dynamics*; 34:1489–1511.
- Krawinkler, H. (2009). Loading histories for cyclic tests in support of performance assessment of structural components. *The 3rd International Conference on Advances in Experimental Structural Engineering*, October 15-16, 2009, San Francisco, CA.
- Lowes, L., Mitra, N., and Altoontash, A., (2004), A Beam-Column Joint Model for Simulating the Earthquake Response of Reinforced Concrete Frames, PEER Report 2003/10, Pacific Earthquake Engineering Research Center.
- Moen, C. D. (2008). *Direct strength design for cold-formed steel members with perforations*. Ph.D. dissertation, Johns Hopkins Univ., Baltimore.
- NI Labview (2005). Labview, Version 8. National Instruments, www.labview.com, Austin, TX
- Mazzoni, S., McKenna, F., Scott, M. H., and Fenves, G. L. (2009). *Open System for Earthquake Engineering Simulation User Command-Language Manual*, OpenSees Version 2.0, Berkeley, California.
- Popov, E. P., Mahin, S. A., and Zayas, V. A. (1979). Cyclic inelastic buckling of thin tubular columns. *Journal of the Structural Division*, 105(11), 2261–2277.
- SFA (2000). Low-rise residential construction details. Publication NT6-00, Steel Framing Alliance. Washington, D.C.
- Usami, T., and Ge, H. B. (1998). Cyclic behavior of thin-walled steel structures—numerical analysis. *Thin-Walled Structures*, 32(1-3), 41-80.